Quantitative histopathologic assessment of perfusion MRI as a marker of glioblastoma cell infiltration in and beyond the peritumoral edema region

Quantitative Histopathologic Assessment of Perfusion MRI as a Marker of Glioblastoma Cell Infiltration in and Beyond the Peritumoral Edema Region

A. Vallatos, PhD,[1,2] H.F.I. Al-Mubarak, BSc,[1,3] J.L. Birch, PhD,[4] L. Galllagher, HND,[1] J.M. Mullin, HND,[1] L. Gilmour, PhD,[4] W.M. Holmes, PhD,[1*] and A.J. Chalmers, PhD[4]

Background: Conventional MRI fails to detect regions of glioblastoma cell infiltration beyond the contrast-enhanced T_1 solid tumor region, with infiltrating tumor cells often migrating along host blood vessels.
Purpose: To quantitatively and qualitatively analyze the correlation between perfusion MRI signal and tumor cell density in order to assess whether local perfusion perturbation could provide a useful biomarker of glioblastoma cell infiltration.
Study Type: Animal model.
Subjects: Mice bearing orthotopic glioblastoma xenografts generated from a patient-derived glioblastoma cell line.
Field Strength/Sequences: 7T perfusion images acquired using a high signal-to-noise ratio (SNR) multiple boli arterial spin labeling sequence were compared with conventional MRI (T_1/T_2 weighted, contrast-enhanced T_1, diffusion-weighted, and apparent diffusion coefficient).
Assessment: Immunohistochemistry sections were stained for human leukocyte antigen (probing human-derived tumor cells). To achieve quantitative MRI-tissue comparison, multiple histological slices cut in the MRI plane were stacked to produce tumor cell density maps acting as a "ground truth."
Statistical Tests: Sensitivity, specificity, accuracy, and Dice similarity indices were calculated and a two-tailed, paired *t*-test used for statistical analysis.
Results: High comparison test results (Dice 0.62–0.72, Accuracy 0.86–0.88, Sensitivity 0.51–0.7, and Specificity 0.92–0.97) indicate a good segmentation for all imaging modalities and highlight the quality of the MRI tissue assessment protocol. Perfusion imaging exhibits higher sensitivity (0.7) than conventional MRI (0.51–0.61). MRI/histology voxel-to-voxel comparison revealed a negative correlation between tumor cell infiltration and perfusion at the tumor margins ($P = 0.0004$).
Data Conclusion: These results demonstrate the ability of perfusion imaging to probe regions of low tumor cell infiltration while confirming the sensitivity limitations of conventional imaging modalities. The quantitative relationship between tumor cell density and perfusion identified in and beyond the edematous T_2 hyperintensity region surrounding macroscopic tumor could be used to detect marginal tumor cell infiltration with greater accuracy.
Level of Evidence: 1
Technical stage: 2

J. MAGN. RESON. IMAGING 2018.

GLIOBLASTOMA (GBM) is the most common and aggressive primary brain tumor. Survival in patients receiving the current standard of care is less than a year after diagnosis.[1] A major factor contributing to treatment failure is the ability of tumor cells to infiltrate normal brain regions,[2] extending several centimeters from the tumor bulk edge.

View this article online at wileyonlinelibrary.com. DOI: 10.1002/jmri.26580

Received Jul 27, 2018, Accepted for publication Oct 26, 2018.

*Address reprint requests to: W.H., Department Glasgow Experimental MRI Centre, Institute of Neuroscience and Psychology, University of Glasgow, Wellcome Surgical Centre, Garscube Estate, Bearsden Road, Glasgow G611QH, UK. E-mail: william.holmes@glasgow.ac.uk.
The last two authors contributed equally to this work.

From the [1]Glasgow Experimental MRI Centre, Institute of Neuroscience and Psychology, University of Glasgow, UK; [2]Centre for Clinical Brain Sciences, University of Edinburgh, UK; [3]University of Misan, Iraq; and [4]Wolfson Wohl Translational Cancer Research Centre, Institute of Cancer Sciences, University of Glasgow, UK

Additional supporting information may be found in the online version of this article.

Infiltration compromises the ability to achieve complete surgical resection of the tumor, thereby contributing to high recurrence rates, and limitations in the ability to accurately image infiltration reduce the accuracy of target volume delineation for radiotherapy planning.[3] It is crucial to develop imaging modalities that enable better tumor delineation; particularly when considering marginal regions with low tumor cell density.

Despite providing rich insights into tumor characteristics, conventional clinical magnetic resonance imaging (MRI) methods such as contrast-agent enhanced T_1 (cT_1), T_2 weighted (T_2), diffusion-weighted (DW), or apparent diffusion coefficient maps (ADC) fail to characterize regions of low density tumor cell infiltration. cT_1 images allow delineation of strongly enhancing regions corresponding to solid tumor with pathologic neovascularization,[4] often surrounding a nonenhancing necrotic core. T_2 imaging commonly reveals extensive regions of abnormality surrounding the cT_1 enhancing lesion. While these regions are associated with edema, several biopsy studies have demonstrated the presence of infiltrating tumor cells within them,[5] with the extent of the hyperintensity region being inversely correlated with survival.[6] Evaluating progression of T_2 to cT_1 abnormalities[7] suggests that high T_2 signal regions could represent an earlier stage of tumor development. However, beyond the cT_1 enhancement region, there is currently no reliable method for probing the extent and density of tumor cell infiltration. Accurate delineation is often compromised by MRI sensitivity limitations related to the fact that marginal tumor cell density is much lower than healthy tissue cellular density.

Several approaches for probing regions of low tumor cell density are currently under investigation. Infiltration of white matter tracts has been extensively characterized by diffusion tensor imaging (DTI), with fractional anisotropy properties being related to infiltration patterns.[8] MR spectroscopy focusing on increased choline peaks[9] has probed the hypermetabolic behavior of tumor cells in the vicinity of the cT_1 enhancement region. Perfusion measurements in the same region tend to show increased values due to early angiogenesis.[10] Despite some promising results, most of these approaches suffer from sensitivity limitations restricting their use to regions of higher tumor cell density, typically adjacent to the cT_1 abnormal region. However, theoretical invasion models accounting for MRI sensitivity suggest that infiltration may often extend beyond abnormal T_2 regions.[11]

Distant from the cT_1 enhancement region, invading tumor cells often progress along blood vessels and in the absence of angiogenesis; co-option[12] tends to be the predominant mechanism by which they access the blood supply. Published data indicate that even individual cells can disrupt the blood–brain barrier (BBB) integrity,[13] thus providing an opportunity to detect tumor infiltration at its earliest stages. Perfusion MRI measurements performed either with the use of contrast agents or by arterial spin labeling (ASL)[14] could allow such effects to be probed. Perfusion MRI is already used to improve GBM delineation and facilitate clinical decision making.[15] Contrast-enhanced techniques such as dynamic susceptibility contrast (DSC) and dynamic contrast enhancement (DCE) are widely used in brain tumor imaging,[16] but their relatively low signal-to-noise ratio (SNR) in infiltrated healthy tissue regions makes subtle perfusion perturbation studies challenging. ASL is noninvasive and has been shown to provide similar results to DSC in brain tumor studies, with fewer susceptibility artifacts.[14] If sufficient SNR could be achieved, this technique, which uses blood water as a marker of perfusion, could be more sensitive to subtle perfusion perturbations in the infiltration zone than other methods, making it a suitable candidate for probing infiltration away from the cT_1 enhancement region.

Robustly assessing the ability of MRI protocols to probe tumor infiltration is another important challenge. Clinical studies using stereotactic biopsy techniques are limited to measurements within regions of T_2 abnormality, relying on MRI for accurate sampling and typically suffering from low precision.[17] Preclinical studies provide an opportunity for more quantitative histopathologic MRI assessment; however, most studies to date have used qualitative approaches, probably due to difficulties with MRI/histology registration.[18] Often, histological slices are not cut in the MRI plane and the enormous difference in slice thickness compared with MRI is ignored (histology ~20 μm, MRI ~1000 μm). The development of new methods for quantitative histopathologic assessment of MRI modalities is crucial in order to analyze infiltrative glioblastoma models, where heterogeneous tumor distributions can vary considerably within the MRI slice thickness.

This study aimed to quantitatively and qualitatively analyze the correlation between perfusion MRI signal and tumor cell density at the tumor margins, to assess whether local perfusion perturbation could provide a useful biomarker of glioblastoma cell infiltration in and beyond the peritumoral edema region.

Materials and Methods

Tumor Model and Experimental Design

Experiments were performed on CD1 nude mice (Charles River Laboratories, Wilmington, MA), in accordance with the local ethical review panel.[19] Mice (20–25 g) were acclimatized at least 1 week prior to any experimental procedure. G7 human glioblastoma cells were cultured in stem-like conditions (Advanced DMEM:F12, containing 20 μM EGF/FGF, 1% B27, 0.5% N2, heparin, 1% L-Glut) on Matrigel-coated plates. The animals were intracranially injected with G7 cells (10^5 cells per mouse) into the subventricular zone using stereotactic equipment.[20] Study outcomes are reported following the ARRIVE guidelines.[21]

Ten animals were scanned 9 and 12 weeks after GBM cell injection. Following MRI, animals were sacrificed and brains were freeze-fixed to minimize macroscopic tissue deformation.[22] MRI assessment was performed using 3D datasets of registered MRI with human leukocyte antigen (HLA) density maps achieved by averaging multiple histological slices evenly distributed in the MRI plane.

Four additional animals were scanned at weeks 12 and 15 to allow the formation of a necrotic core. Following MRI, the animals were sacrificed and brains were paraffin-embedded to minimize microscopic deformation of cells to allow high-resolution histology analysis.

MRI Setup and Acquisition

MRI experiments were performed on a Bruker Biospec Avance 7T imaging system with a 30-cm horizontal bore (Bruker, Ettlingen, Germany). Homogeneous RF excitation was achieved using a birdcage volume resonator (diameter = 72 mm, length = 110 mm) and an actively decoupled 4-channel phased array receive-only head surface coil was used for signal detection (Rapid Biomedical, Wurzburg, Germany). The system was equipped with shielded magnetic field gradients producing up to 400 mT m^{-1}.

The animals were anaesthetized using 5% isoflurane and a 30:70 O_2/N_2O ratio before being positioned prone on an MRI animal cradle. A hot water circulation jacket was used to regulate physiological temperature (37 ± 1°C). The head was secured laterally by conical ear rods and longitudinally by the nose cone used for anesthetic gas delivery. The animals breathed spontaneously through a facemask, with isoflurane delivered at a constant flow mixed with a 40:60 ratio of O_2/N_2O (1 L min^{-1}). Isoflurane concentration was varied (1.5–3%) in order to maintain stable respiration rates within normal physiological ranges (40–70 bpm). Respiration was monitored using a pressure sensor connected to an air-filled balloon placed under the animal abdomen (Biotrig Software, Bruker).

Following a geometry-correction sequence, a series of MRI experiments were performed (field of view 2 × 2 cm, five 1.5 mm coronal imaging slices centered at 4 mm posterior from rhinal fissure). T_2-weighted imaging was performed using a rapid acquisition with relaxation enhancement (RARE) sequence (echo time [TE] = 47 msec, repetition time [TR] = 4,300 msec, matrix = 176 × 176, 9 min). Higher-resolution T_2 images (slice thickness = 0.5 mm) were acquired during the final scanning session. Diffusion-weighted imaging (DWI) was performed using a 4-shot spin-echo planar imaging DW scan (TE = 20 msec, TR = 4,300 msec, matrix = 128 × 128, six directions, b-values = 0, 1000 s mm^{-2}, 10 min). Perfusion weighted imaging (PWI) was performed using an optimized multiple boli arterial spin labeling sequence (mbASL),[23] labeling with a train of 20 hyperbolic-secant inversion pulses (duration = 3.3 msec, dimensionless amplitude parameter μ = 8, angular modulation β = 760 s^{-1}) evenly distributed over 5 seconds (postlabeling delay = 50 msec). The inversion slice width was 8.5 mm and the offset from the imaging slice was 15 mm. Image acquisition was achieved with an 4-shot EPI module (TE = 12 msec, TR = 7 sec, matrix = 96 × 96, partial FT = 1.4, 12 averages, 9 min). Finally, contrast-enhanced T_1 imaging (cT_1) was performed using a RARE acquisition (TE = 12.3 msec, TR = 800 msec, matrix = 176 × 176, 8 min). Images were acquired before and 5 minutes after gadolinium-DTPA injection. Following animal scanning, MRI experiments were repeated on a doped water phantom used for correcting receiver coil bias. Data were exported in DICOM format.

Histology Protocols

FREEZE-FIXATION. Following MRI, anesthetized mice received an intravenous injection of 0.1 ml 7.5 mg ml^{-1} 70 kDa Texas red-labeled dextran (Thermo Fisher Scientific, UK) in phosphate-buffered saline (PBS), for subsequent brain perfusion analysis. Two minutes following injection, mice were sacrificed and brains were removed and fresh-frozen. Brain slicing was performed manually on an OTF 5000 Bright cryostat, guided by high-resolution T_2 images. The identification of common features by an experienced neuroscience research technician (L.G., 20 years experience) allowed positioning the sectioning plane parallel to the MRI plane. Interleaved 20 μm and 60 μm sections were cut. The 20-μm cryosections were fixed in ice-cold acetone and washed in PBS before blocking in 3% BSA/TBS/0.05% Tween for 30 minutes at room temperature. A 1:500 dilution HLA antibody (Abcam, Cambridge, MA; ab70328) in blocking buffer was added and incubated for 2 hours at room temperature. Sections were washed three times with TBS-Tween before addition of 1:1000 antimouse Alexa 647-conjugated secondary antibody (A-21236, Thermo Fisher Scientific) for 1 hour incubation in the dark. Sections were washed three times with TBS-Tween and mounted in ProLong Diamond Antifade mount with DAPI (P36966, Thermo Fisher Scientific). Whole-brain section tile scans were conducted using a Zeiss (Thornwood, NY) 710 upright confocal microscope. For dextran imaging, unfixed 60-μm cryosections were imaged by z-stack tile scanning on a Zeiss 710 upright confocal microscope. Images were exported as a .tiff.

PARAFFIN EMBEDDING. Mice were sacrificed and brains dissected, cut in half through the tumor injection site, formalin-fixed, paraffin-embedded, and sectioned (4 μm). Sections were stained for hematoxylin and eosin (H&E), Ki67, or incubated with 1:500 dilution HLA antibody (Abcam ab70328) and visualized using DAB staining (Dako EnVision + System HRP [DAB] K4007) followed by counterstaining and mounting. Sections were imaged using a Hamamatsu (Bridgewater, NJ) Nanozoomer Slide scanner with Leica SlidePath imaging Software (J.B., 8 years experience) or tiling at ×10 on a Zeiss Axio microscope.

Image and Data Analysis

Figure 1 summarizes the protocol for the production of 3D datasets used for MRI assessment. The most critical steps are highlighted in Supporting Fig. 1. Data were processed using MatLab R2015a (MathWorks, UK) code developed in-house.

MRI. Surface-coil sensitivity correction was performed on T_2 and DW data by dividing by the phantom data.[24] Normalized relative perfusion maps (PW) were achieved by

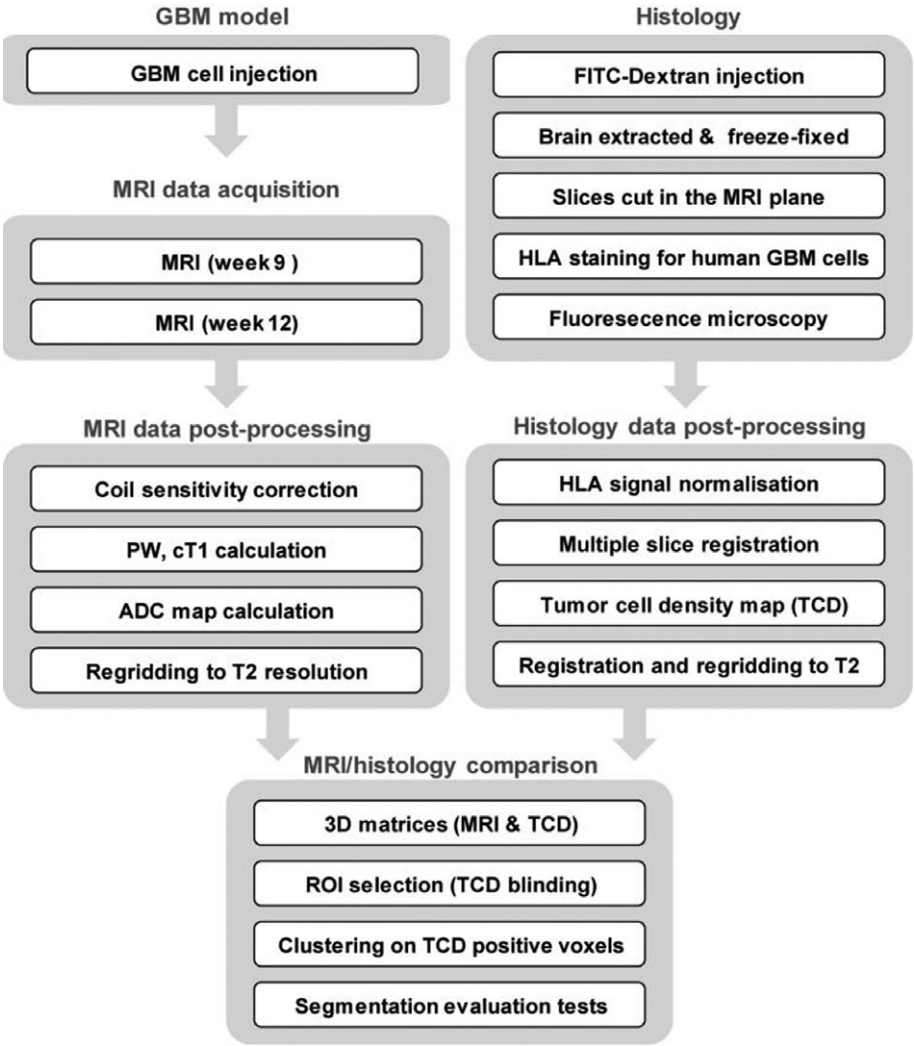

FIGURE 1: Simplified diagram of the pipeline leading to the production of 3D matrices combining MRI and histology data. Quantitative evaluation of MRI segmentation was achieved by comparing MRI and tumor cell density maps from the resulting dataset.

subtracting the control and label images acquired with different states of arterial blood magnetization, and dividing by the control,[25] $(M_{control} - M_{label}) / M_{control}$. Contrast-enhanced images (cT_1) were achieved by subtracting T_1 acquisitions before and after Gd injection, and normalizing by T_1 data acquired before injection, $(M_{postGd} - M_{preGd}) / M_{preGd}$. ADC maps were calculated by fitting the data to the monoexponential Stejkal–Tanner equation. All data were resized to T_2 resolution (176 × 176) and a mask was applied to null extra-brain regions.

HISTOLOGY. Histology slice images exported from fluorescence microscopy were registered, resized to MRI data, and normalized using the RGB histogram method. Three to five slices (interslice distance ~0.3 mm) distributed across the MRI slice were averaged to produce tumor cell density maps (TCD), where signal intensity is proportional to the intravoxel concentration of tumor cell cytoplasm. MRI-TCD registration was performed using an affine intensity-based scheme (mutual information method).

IMAGE SEGMENTATION. Tumor-related abnormal regions of interest (ROIs) probed by each imaging modality were manually drawn by H.F.I.A. and A.V. (3 and 5 years experience, respectively) in the region where the TCD map was produced. PW segmentation was facilitated by comparison with healthy mice PW images (Supporting Fig. 2). MRI ROI delineation was performed without prior knowledge of the histology data, to avoid selection bias. Care was taken not to include noninvasion-related enhancement (eg, ventricle compression). Animals that did not exhibit tumor growth (n = 1) were removed from the study, while animals with necrotic lesions were not considered for voxel-to-voxel comparison with TCD maps (n = 2). Histology ROIs were selected on the basis of HLA stain intensity on TCD maps. To minimize HLA staining artifacts, manual selection was favored to a user-independent intensity-based selection. Clustering

separating high and low tumor density regions within TCD ROIs (A.V. ROI selection) was performed using a Gaussian mixture model.[26]

Statistical Analysis

TCD ROIs were considered as the "ground truth" for evaluating MRI ROIs. Interobserver reproducibility was quantified using the coefficient of variation (CV), calculated for each lesion by 100 × standard deviation/mean, and averaged for each imaging modality. Sensitivity, specificity, accuracy, and Dice similarity indices[27,28] were calculated for each animal and imaging modality. Two-tailed Student's *t*-test was used for comparisons between MRI tumor regions and histology tumor region. All values are reported as mean ± standard deviation. Boxplots show the mean (black line), median (blue line), $25^{th}/75^{th}$ percentiles (box), and extreme points (whiskers) not considered outliers (within 1.5 times the interquartile range). Raw data (red dots) were jittered along x. Statistical significance flags: $*P < 0.05$, $**P < 0.01$, $***P < 0.001$, $****P < 0.0001$, and NS not statistically significant.

Results

Marginal Infiltration Model

Figure 2a shows T_2 and cT_1 images obtained from the same animal at 12 and 15 weeks postinjection. At week 15 all cT_1 images presented a nonenhancing necrotic core surrounded by a contrast-enhancing region identified as solid tumor. Regions of abnormal T_2 signal were systematically larger than cT_1, with the mismatch often identified as low density tumor cell infiltration in the healthy tissue (Fig. 2b(ii)). Figure 2c shows T_2 and cT_1 images obtained from three animals at 12 weeks postinjection. While significant abnormal volumes are visible on T_2, most cT_1 showed no significant signal change. Only three cases of minor cT_1 contrast enhancement in the brain region were identified at week 12 (eg, Fig. 2c (iii)) and necrotic cores were either very small or invisible. Note that at these earlier timepoints, T_2 abnormalities appeared more homogeneous and were of similar volume among animals (Supporting Fig. 3a–c), while after week 12, tumor growth varied significantly between animals and weight loss was observed in some (Supporting Fig. 3c,d).

PW Detects More Extensive Regions of Tumor Infiltration Than Conventional MRI

Representative images obtained at weeks 9 and 12 during the longitudinal MRI study are shown in Fig. 3a,b. Most techniques detected a tumor-related region of abnormality by week 9. Tumor-related lesions remained homogeneous until week 12 and appeared as hyperintense on T_1, T_2, and DW and hypointense on ADC and PW. Only two cases exhibited

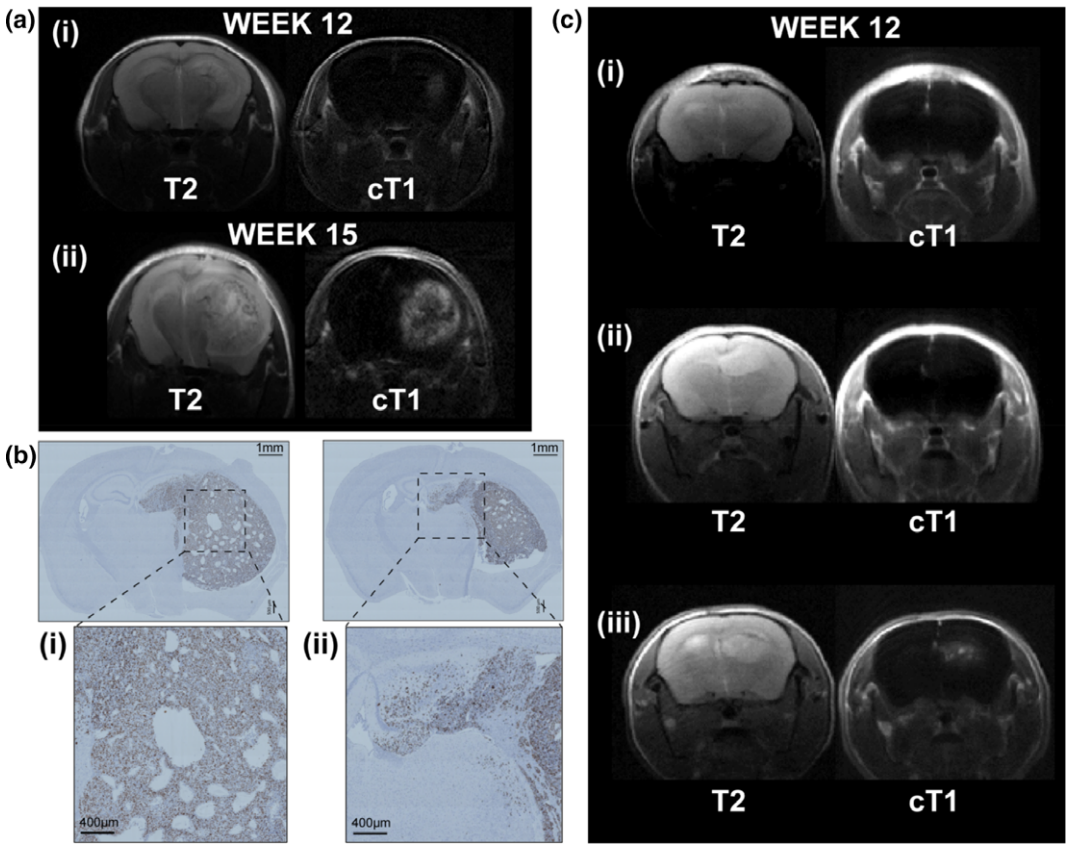

FIGURE 2: (a) T_2-weighted and contrast-enhanced T_1 images at 12 (i) and 15 (ii) weeks postinjection for the same animal. (b) Ki67 immunohistochemistry on slices obtained from the animal shown in (a), within the MRI image plane and 0.8 mm apart (magnification ×10). Regions of necrosis (i) and infiltration (ii) are highlighted. (c) T_2-weighted and contrast enhanced T_1 images obtained 12 weeks postinjection.

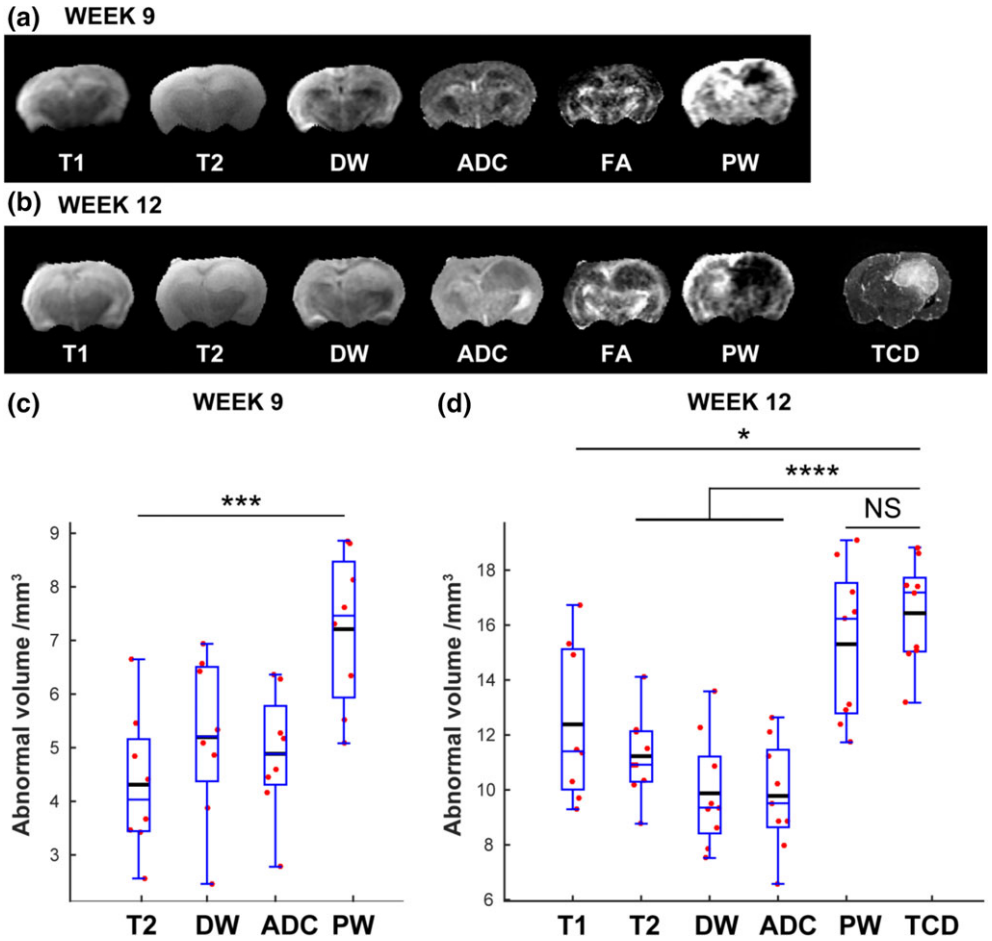

FIGURE 3: Images from different MRI modalities at weeks 9 (a) and 12 (b) postinjection. cT_1 values were not included since only three mice exhibited cT_1 enhancement at this stage. Week 12 also includes the tumor cell density map (TCD) obtained for the same brain region. The displayed PW contrast was adjusted to allow clearer differentiation within the invasion area. Tumor-related abnormal volumes measured 9 weeks (c) and 12 weeks (d) postinjection (n = 9).

small necrotic cores at this stage of tumor progression (high ADC in the tumor core). FA values were low in tumor core regions, characteristic of both edema and isotropic tumor proliferation, and high in tumor margin regions. At week 12, a strong similarity was observed between the abnormal regions identified by the different MRI modalities and the regions of high tumor cell concentration identified on tumor cell concentration maps (TCD). Supporting Fig. 4 shows the corresponding MRI ROIs. Interobserver CV at week 9 was 29% for T_2, 12% for DWI, and 19% for ADC and PW. At week 12, CV was 20% for T_1 and T_2, 21% for DWI, 19% for ADC, 12% for PW, and 10% for TCD maps.

Figure 3c,d shows the average volumes of tumor-related abnormal regions for each imaging modality (including tumor cell density maps) at 9 and 12 weeks postinjection of G7 cells. At both timepoints, PW imaging exhibited significantly larger abnormal regions than relaxation (T_1, T_2) or diffusion-based (DW, ADC) MRI techniques. For week 9, the results have to be considered cautiously, as the lesions are relatively small and the resizing of lower-resolution imaging modalities (eg, PW) can introduce increases of the abnormality-related ROI. Considering a Gaussian infiltration front (Supporting Fig. 5), the resulting ROI error was estimated at about 10% for the smaller lesions of this work (week 9) and below 1% for medium and large lesions (week 12). Note that this error is small compared to the T_2/PW abnormal volume ratio (~60% on week 9 and ~75% on week 12).

The 3D matrices allow a quantitative evaluation of MRI techniques in comparison with the "ground truth" provided by the TCD maps. While no significant difference between PW abnormal volumes and TCD volumes was observed (P = 0.2), abnormal volumes detected by all other imaging techniques were significantly smaller. Figure 4 shows the results of various segmentation evaluation tests applied to the volume calculation ROIs.

All segmentations achieved relatively high Dice scores and accuracy indices[27] (Fig. 4a,b), highlighting the quality of the quantitative histological evaluation protocol. While PW segmentation achieved the highest Dice score, with T_2 and ADC providing with the best results among standard MRI protocols, Dice score differences did not reach statistical significance (P = 0.2 for t-test comparison between PW and T_2

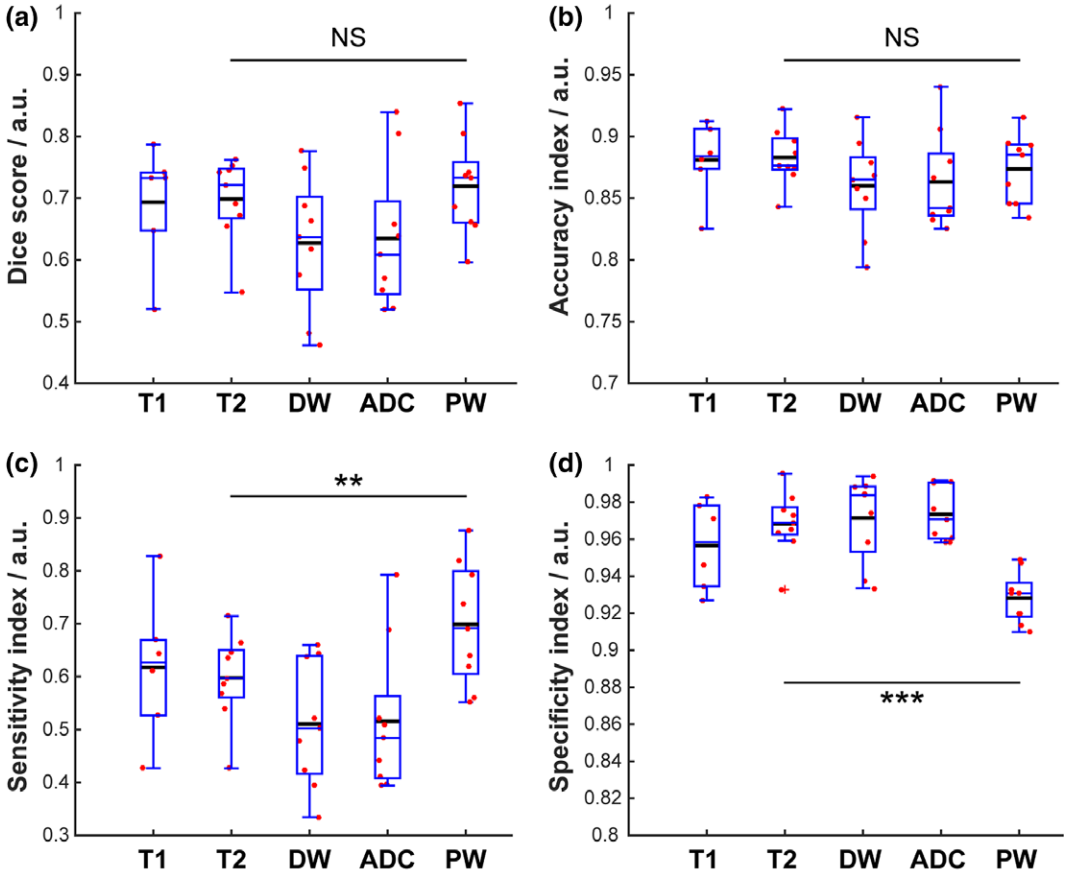

FIGURE 4: Dice score (a), accuracy index (b), sensitivity index (c), and specificity index (d) achieved for the segmentation of each imaging modality at week 12, in comparison with TCD segmentation ("ground truth"). ROIs were the same as for the volume analysis shown in Fig. 3.

Dice score distributions). However, PW was associated with significantly higher sensitivity than other techniques (Fig. 4c). Conversely, relaxation and diffusion-based imaging showed higher specificity than perfusion (Fig. 4d). This reflects, first, the fact that standard MRI protocols underevaluate tumor volume and, second, that, while average PW ROI volume (15 ± 3 mm^3) was similar to the average TCD ROI volume (16 ± 2 mm^3), in three cases PW ROI volumes were found to be greater than TCD ones (by 13%, 8%, and 3%).

Relationship Between Perfusion and Invasion in Tumor Margin Regions

Histological analysis was performed to better characterize the relationship between perfusion and tumor cell infiltration. Figure 5a shows a comparison between histological slices probing the perfusion/delivery of FITC-dextran 70 kDa and slices from the same animal stained for HLA, in the same region as the MRI images shown in Fig. 3a,b. As expected, there is a strong relationship between PW imaging and FITC-dextran staining, with regions of hypoperfusion clearly demarcated by both techniques. Regions of increased tumor cell density exhibited reduced perfusion in both PW and dextran assays; this was also highlighted by the similarity test results comparing TCD ROI with PW ROI (Fig. 4a,b).

This relationship between perfusion and infiltration was stronger in marginal regions of lower tumor cell density. This is highlighted by the dataset from one mouse that developed two distinct tumor lesions (Fig. 5b): a high-density lesion (near the tumor cell injection point) surrounding a small necrotic core (white spots on T_2 and ADC; black spots on HLA) and a more homogeneous, low tumor density lesion that appeared later in tumor development. The physical connection between the two lesions, occurring at the back of the brain, is indicated by the red arrows on the T_2 images shown in Fig. 5b(ii). While both PW and dextran images show a reduction in perfusion in the newly infiltrated lower region, the relation between dextran delivery and invasion is less clear around the necrotic core of the main lesion.

Histological analysis of formalin-fixed tissue allows better understanding of the cellular mechanisms underlying the relationship between marginal tumor infiltration and perfusion. Figure 5c,d shows histological images derived from G7 tumor edges. The combination of H&E and tumor cell-specific HLA staining revealed that several blood vessels at the tumor margins were surrounded by tumor cells. In some

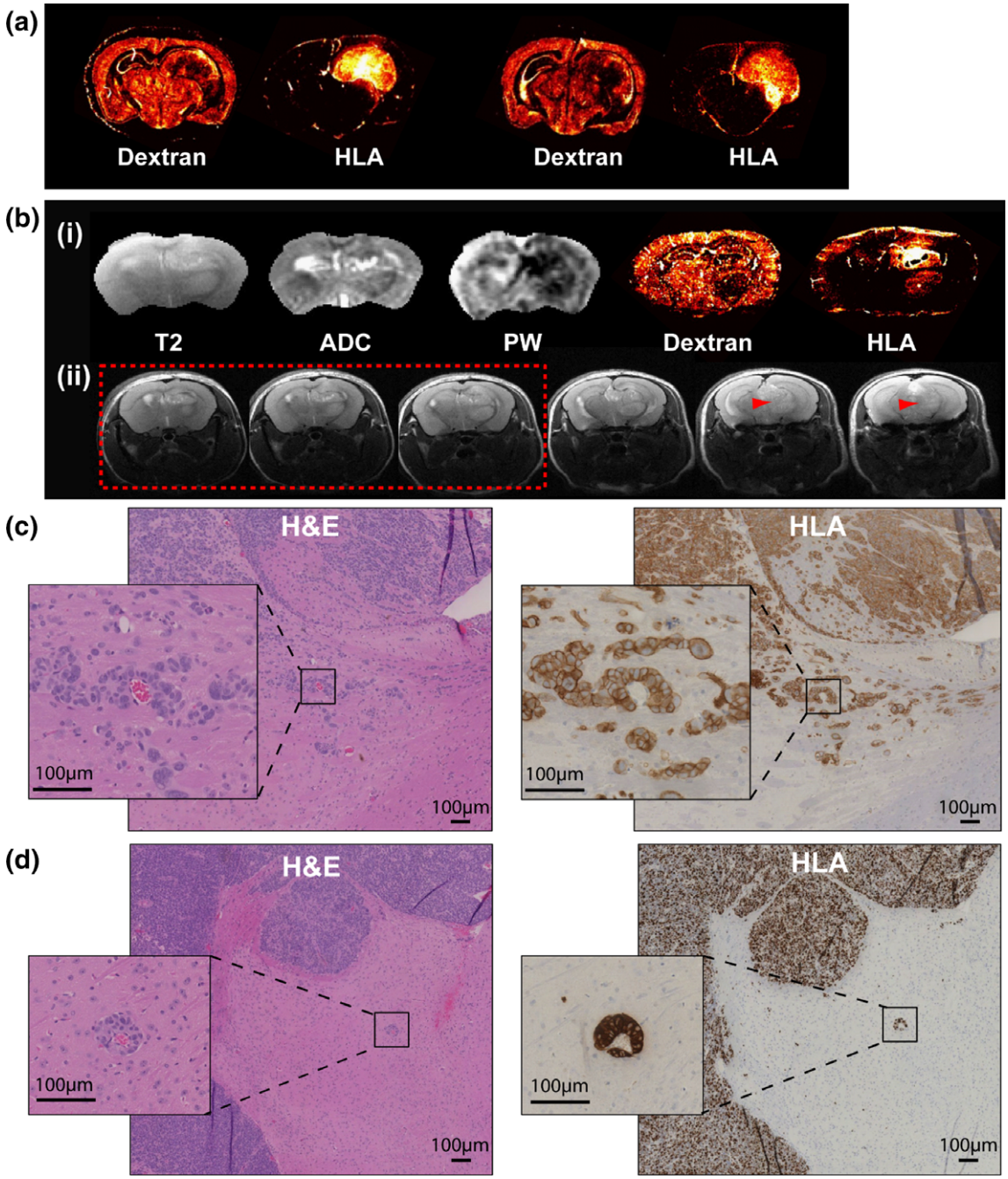

FIGURE 5: (a) Fluorescence microscopy images probing HLA and dextran 70 kDa at two different locations within the MRI slices shown in Fig. 3B (magnification ×10). (b) (i) MRI (T_2, ADC, PW) and fluorescence microscopy images (HLA, dextran) from a mouse at 12 weeks postinjection (ii) T_2 images of thickness 0.5 mm acquired at the same timepoint. The red doted box highlights the three 0.5-mm thick T_2 slices acquired at the same location as the T_2 image shown in Fig. b (i). The red arrows show connection points between the upper and the lower tumor lesion. (c,d) Tumor margin samples of brains stained for H&E and HLA. Regions of vascular cuffing by invading tumor cells are enlarged.

cases, vascular cuffing by invading tumor cells was observed at locations remote from the tumor front (Fig. 5d).

Perfusion Variation as a Marker of Tumor Cell Infiltration

The high values of the segmentation evaluation indices (Fig. 4) indicate good agreement between MRI and histology datasets, enabling voxel-to-voxel comparison between MRI modalities and TCD maps to be undertaken. PW and TCD images for each animal (Fig. 6a) were used to produce scatterplots of perfusion against tumor cell density (Fig. 6b). Tumor-positive voxels (TCD ROI) are highlighted (red points). At the interface between healthy brain and tumor infiltration regions, voxels of extremely low tumor cell density exhibit similar PW values to voxels that are outside the tumor infiltration regions. As suggested by the histology data analysis

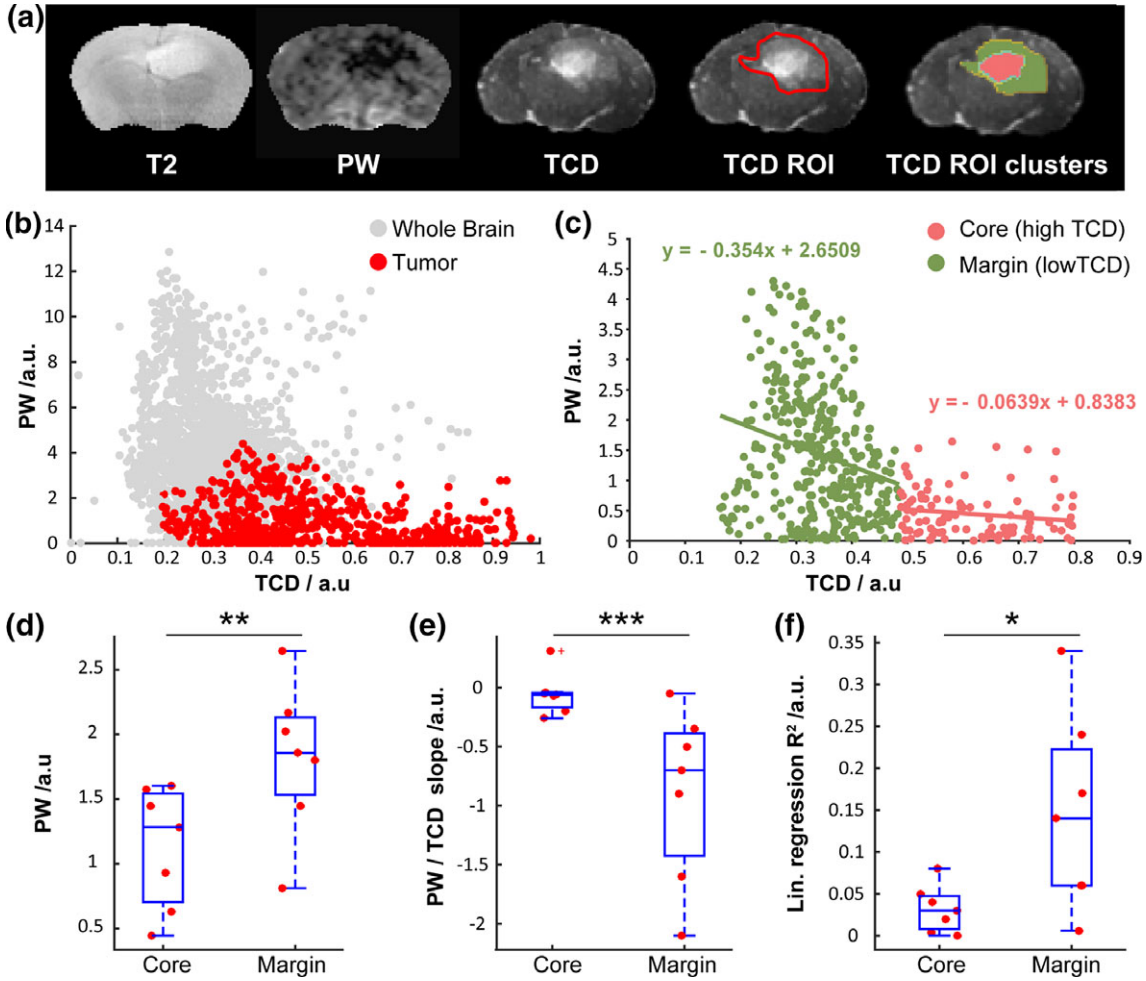

FIGURE 6: (a) T_2, PW and TCD images from a single animal. TCD ROI selection in red indicates the manually segmented tumor-positive region of the brain. Clustering of high and low TCD values was used to separate core and marginal tumor regions. (b) Scatterplots of PW signal against TCD for each voxel in the images shown in (a); red points correspond to voxels situated within the TCD ROI tumor positive region. (c) Scatterplots of PW signal against TCD for the tumor-positive voxels only. Linear regression fits were applied separately on data from the core and marginal tumor regions obtained by the tumor region clustering shown in (a). "Core" and "margin" region boxplots show the average PW signal (d), linear regression fit slope (e), and R^2 of the fit (f) (n = 7).

(Fig. 5), perfusion was generally high in low TCD value voxels, and decreased with increasing TCD. This indicated that the voxel-to-voxel approach could be applied to further characterize the relationship between perfusion and invasion at the tumor margins. This was achieved by comparing high TCD "tumor core" regions, typically situated around the G7 cell injection point, with low TCD "tumor margin" regions. To separate these regions, clustering analysis was performed on the tumor-positive regions of the TCD maps (Fig. 6a). By focusing on the tumor region and plotting TCD against PW intensity for each voxel (Fig. 6c), we generated a semiquantitative representation of the relationship between tumor burden, as quantified by TDC, and local perfusion. On this graph, marginal voxels (green) exhibit significantly lower average TCD values than core voxels (pink). Importantly, these marginal voxels exhibit significantly higher perfusion values than core voxels (Fig. 6d). The relation between perfusion and invasion at the margins was quantified by applying separate linear regression fits to the "core" and the "margin" voxel datasets (Fig. 6c). A significant negative correlation between tumor infiltration and perfusion was observed at the tumor margins (where tumor cell infiltration of the normal brain occurs), while no clear relationship was identified in tumor core regions (Fig. 6e). Consistent with this, linear regression R^2 values were significantly higher for margin datasets (Fig. 6f).

Discussion

This study demonstrated the existence of an MRI-detectable relationship between tumor cell infiltration and local perfusion in tumor margin regions of an orthotopic glioblastoma model that recapitulates imaging and histopathological features of the human disease. To achieve this, we interrogated our in vivo model, which exhibits infiltrative tumor margins,

using a high SNR ASL sequence and a novel MRI validation approach based on the use of multiple histology slices in the MRI plane.

Great care was taken in confirming the clinical relevance of the G7 marginal tumor infiltration model. First, this highly infiltrative model exhibits sizeable regions of low tumor cell density that are not probed by cT_1 and which extend into and beyond the regions of abnormal T_2 signal. In addition, the relatively slow rate of progression of the G7 model enables considerable cell infiltration to take place, recapitulating the clinical scenario where edema/infiltration T_2 lesions are systematically larger than cT_1 lesions. By contrast, frequently reported GBM models, where tumor cells poorly infiltrate the depth of the brain tissue, exhibit a sharp transition between tumor bulk and healthy brain regions, resulting in similar sized T_2 and cT_1 lesions.[18] Without infiltration, tumor growth resembles that of cells injected in avascular spaces, where the lack of host blood vessels is associated with angiogenesis at very early stages in tumor development.[29] As a consequence, these poorly infiltrative models tend not to reproduce the clinically observed difference between cT_1 and T_2 growth patterns.[30]

Reproducing a realistic marginal invasion microenvironment is another important challenge. In the clinical context, marginal infiltration typically occurs outside contrast-enhancing regions, in a quasinormoxic microenvironment. Perfusion drops with increasing distance from the contrast-enhancing part of the tumor partly due to limited angiogenesis.[31] The vascular endothelial growth factor (VEGF) secreted by GBM cells appears to be involved not only in neovascularization but also in edema production[32] through the induction of vascular permeability.[33] Distant from the hypoxic microenvironment of the tumor core, brain tumors may develop and grow using vascular co-option as the main mechanism of neovascularization,[33] without needing an angiogenic switch.[34,35] Such co-option mechanisms, widely documented in clinical specimens, have been shown to compromise the efficacy of treatments that either target angiogenesis[36] or promote vascular normalization or integrity[37] in both primary and metastatic tumors. Consistent with the clinical context, G7 tumor cells have been shown to express VEGF both in vivo and in vitro[20]; hence, angiopoiesis is expected close to the tumor core. Here, investigating at earlier stages of tumor development allowed minimizing the effects related to tumor angiogenesis or necrosis. Decreased perfusion in tumor regions is commonly observed in rodent glioblastoma models and can be explained by the early stage of tumor progression, before contrast-enhancement related to leaky vessels that arise from angiogenesis. In fact, newly formed tumor vessels are often nonfunctional, displaying low blood flow or not participating in the microcirculation.[31,32] Functional angiogenesis requires solid tumor conditions (eg, significant tumor burden, hypoxia), that can be observed either in noninfiltrative models that lack clinical relevance, or when the tumors reach such large sizes that animal survival and welfare is compromised. Infiltrative preclinical models typically exhibit a detectable reduction in perfusion within the tumor lesion.[18] The infiltrative nature of the G7 model simultaneously ensures reliance on intact host blood vessels[34] and delays development of hypoxic tumor core conditions that induce angiogenesis, thus allowing accurate modeling of the invasive border of GBM.

Despite the clear relationship between tumor cell density and perfusion shown in this work, a direct connection cannot be assumed and several potential mechanisms should be considered. Compression of the peritumoral tissue caused by edema in conjunction with increased intracranial pressure (ICP) is a known cause of reduced local perfusion with increasing distance from the contrast-enhancing part of the tumor.[31] ICP effects are expected to be minimal in this marginal infiltration model due to the relatively small tumor volumes. On the other hand, infiltrated tumor burden could cause healthy tissue compression leading to perfusion drop. Of note, both tumor infiltration and the observed reduction in perfusion extend beyond the detectable T_2 lesion. Finally, infiltration along vascular pathways, as seen in the G7 model, can affect perfusion by both co-option mechanisms and VEGF vascular fenestration effects, as discussed earlier. These potential underlying causes of the observed relationship will be explored in future studies.

Marginal glioblastoma infiltration is difficult to probe and evaluate. It challenges MRI sensitivity limits and often exhibits inhomogeneous spatial distributions that compromise conventional histological validation approaches. In this study, the latter challenge was addressed by developing a method for quantitative MRI assessment using a stack of in-plane histology slices. This method allowed the quantitative evaluation of a range of MRI techniques. T_2 sensitivity limits were highlighted, with abnormal T_2 signal shown to significantly underevaluate tumor infiltration. The high specificity of T_2 in comparison with TCD maps reveals that most abnormal T_2 regions correspond to regions of tumor infiltration. This relationship between high T_2 signal and invasion is in agreement with clinical findings, both with histological data showing high infiltration in the high T_2 signal region surrounding cT_1 enhancement[5] and patient survival analysis showing a negative correlation with abnormal T_2 volume.[35]

In this marginal infiltration model, perfusion MRI measurements detected larger lesions than any other MRI sequence, suggesting that perfusion could be used as a marker of low tumor cell density regions. However, it is important to consider how these findings may be translated to clinical management of GBM. Clinical studies involving perfusion MRI tend to focus on regions surrounding cT_1 enhancement where higher signal is expected because of angiogenesis. This approach minimizes the SNR issues and enables studying

biopsy-compatible regions, but fails to detect marginal infiltration. However, studies can be found where cerebral blood flow was measured in more remote regions. Lin et al[36] measured a negative perfusion gradient at the margins of metastatic lesions that could be related to the co-option/edema mechanisms discussed in this work. The significant relationship observed between infiltrating tumor burden and perfusion at the margins suggests that probing abnormal perfusion gradients far from the cT_1 enhancement regions could facilitate the characterization of marginal glioblastoma infiltration into healthy tissue. The sensitivity of the approach will be strongly dependent on the SNR of the perfusion MRI used. While in high SNR perfusion images the perfusion gradient could be used as a direct marker of tumor cell infiltration into the healthy tissue, lower SNR perfusion images could still potentially be used to produce tumor infiltration probability maps. It is also crucial to consider the impact of alternative, clinically relevant causes of local perfusion perturbation, such as radiation therapy and surgery, which may limit the applicability of this technique to pretherapy planning. However, the ability of this approach to improve tumor delineation at the initial treatment planning stage would be of enormous value, and might lead to better responses to first-line surgery and radiation therapy.

This study was, by necessity, subject to certain limitations that we have sought to address, both in its design and also through consideration of its potential for clinical translation. First, our analysis used a relatively small number of mice, mainly imposed by the time-consuming data acquisition and histology-processing protocols. This was counterbalanced by the introduction of a quantitative histopathologic assessment method that enabled collection of high-quality data from each mouse, and our main findings exhibited robust statistical significance. Another limitation relates to differences between tumor and vessel growth between human gliomas and the G7 model in which tumors grow in the brains of immunodeficient mice. We contend that immune status is unlikely to have a significant effect on the analysis of the relation between local perfusion and tumor burden proposed here. In fact, the tumor-related perfusion drop was related to infiltration through the biomechanical effect of vascular co-option and/or edema, which are clinically relevant mechanisms. To minimize intracranial pressure and vascular compression effects, tumor size was generally limited to less than 10% of total brain volume. This also increased the relevance of evaluation tests requiring significant difference between tumor volume and brain volume.[27] Finally, there are MRI specificities in this work that should be emphasized. The combination of a 7T instrument with a novel perfusion sequence allowed us to overcome SNR limitations of clinical perfusion imaging based on ASL sequences, enabling the study of low perfusion regions. This advantage was counterbalanced by the need to use much higher resolution than in a clinical context in order to properly resolve the perfusion distribution within the mouse brain. Hence, it is important to recognize that alternative perfusion MRI techniques (eg, DSC) could be more efficient in probing infiltration in a clinical context.

In conclusion, this work identified a negative relationship between tumor cell burden and perfusion MRI signal in infiltrative areas of low tumor cell density distant from regions of cT_1 enhancement. The robust protocol that we developed to assess the performance of a range of MRI modalities at the tumor margins constitutes a significant step toward quantitative evaluation of the ability of MRI protocols to probe regions of low tumor cell density. Our results indicate that the relationship between perfusion gradient and tumor cell density has potential as a marker of tumor infiltration. Future work will concentrate on assessment of the clinical relevance of these findings.

Acknowledgment

Contract grant sponsor: The Brain Tumour Charity; Contract grant number: 26/160.

H. Al-Mubarak thanks the Ministry of Higher Education and Scientific Research in Iraq for financial support.

References

1. Johnson DR, Omuro AMP, Ravelo A, et al. Overall survival in patients with glioblastoma before and after bevacizumab approval. J Clin Oncol 2016;34:15.
2. Price SJ, Gillard JH. Imaging biomarkers of brain tumor margin and tumor invasion. Br J Radiol 2011;84:S159–S167.
3. Niyazi M, Brada M, Chalmers AJ, et al. ESTRO-ACROP guideline "target delineation of glioblastomas." Radiother Oncol 2016;118:35–42.
4. Earnest F, Kelly PJ, Scheithauer BW, et al. Cerebral astrocytomas — Histopathologic correlation of MR and Ct contrast enhancement with stereotactic biopsy. Radiology 1988;166:823–827.
5. Eidel O, Burth S, Neumann JO, et al. Tumor infiltration in enhancing and non-enhancing parts of glioblastoma: A correlation with histopathology. PLoS One 2017;12:e0169292.
6. Schoenegger K, Oberndorfer S, Wuschitz B, et al. Peritumoral edema on MRI at initial diagnosis: An independent prognostic factor for glioblastoma? Eur J Neurol 2009;16:874–878.
7. Radbruch A, Lutz K, Wiestler B, et al. Relevance of T2 signal changes in the assessment of progression of glioblastoma according to the Response Assessment in Neurooncology criteria. Neuro-Oncol 2012;14:222–229.
8. Mori S, Frederiksen K, Van Zijl PCM, et al. Brain white matter anatomy of tumor patients evaluated with diffusion tensor imaging. Ann Neurol 2002;51:377–380.
9. Sijens PE, Oudkerk M. H-1 chemical shift imaging characterization of human brain tumor and edema. Eur Radiol 2002;12:2056–2061.
10. Henry RG, Vigneron DB, Fischbein NJ, et al. Comparison of relative cerebral blood volume and proton spectroscopy in patients with treated gliomas. Am J Neuroradiol 2000;21:357–366.
11. Swanson KR, Bridge C, Murray JD, Alvord EC. Virtual and real brain tumors: using mathematical modeling to quantify glioma growth and invasion. J Neurol Sci 2003;216:1–10.

12. Holash J, Maisonpierre PC, Compton D, et al. Vessel cooption, regression, and growth in tumors mediated by angiopoietins and VEGF. Science 1999;284:1994–1998.

13. Watkins S, Robel S, Kimbrough IF, Robert SM, Ellis-Davies G, Sontheimer H. Disruption of astrocyte-vascular coupling and the blood-brain barrier by invading glioma cells. Nat Commun 2014;5.

14. Jarnum H, Steffensen EG, Knutsson L, et al. Perfusion MRI of brain tumors: a comparative study of pseudo-continuous arterial spin labelling and dynamic susceptibility contrast imaging. Neuroradiology 2010;52: 307–317.

15. Geer CP, Simonds J, Anvery A, et al. Does MR perfusion imaging impact management decisions for patients with brain tumors? A prospective study. Am J Neuroradiol 2012;33:556–562.

16. Shiroishi MS, Castellazzi G, Boxerman JL, et al. Principles of T-2*-weighted dynamic susceptibility contrast MRI technique in brain tumor imaging. J Magn Reson Imaging 2015;41:296–313.

17. Jackson RJ, Fuller GN, Abi-Said D, et al. Limitations of stereotactic biopsy in the initial management of gliomas. Neuro-Oncol 2001;3: 193–200.

18. Cha S, Johnson G, Wadghiri YZ, et al. Dynamic, contrast-enhanced perfusion MRI in mouse gliomas: Correlation with histopathology. Magn Reson Med 2003;49:848–855.

19. Workman P, Aboagye EO, Balkwill F, et al. Guidelines for the welfare and use of animals in cancer research. Br J Cancer 2010;102:1555–1577.

20. Gomez-Roman N, Stevenson K, Gilmour L, Hamilton G, Chalmers AJ. A novel 3D human glioblastoma cell culture system for modeling drug and radiation responses. Neuro-Oncol 2017;19:229–241.

21. Kilkenny C, Browne WJ, Cuthill IC, Emerson M, Altman DG. Improving bioscience research reporting: The ARRIVE Guidelines for Reporting Animal Research. PLoS Biol 2010;8.

22. Dorph-Petersen KA, Nyengaard JR, Gundersen HJG. Tissue shrinkage and unbiased stereological estimation of particle number and size. J Microsc Oxford 2001;204:232–246.

23. Vallatos A, Gilmour L, Chalmers AJ, Holmes WM. Multiple boli arterial spin labelling for high signal-to-noise rodent brain perfusion imaging. Magn Reson Med 2018;79:1020–1030.

24. Axel L, Costantini J, Listerud J. Technical note — Intensity correction in surface-coil MR imaging. Am J Roentgenol 1987;148:418–420.

25. Noguchi T, Yoshiura T, Hiwatashi A, et al. Perfusion imaging of brain tumors using arterial spin-labeling: Correlation with histopathologic vascular density. Am J Neuroradiol 2008;29:688–693.

26. McLachlan GJ, Peel D. *Finite mixture models*. New York: John Wiley & Sons; 2000.

27. Garcia-Lorenzo D, Francis S, Narayanan S, Arnold DL, Collins DL. Review of automatic segmentation methods of multiple sclerosis white matter lesions on conventional magnetic resonance imaging. Med Image Anal 2013;17:1–18.

28. Zou KH, Warfield SK, Bharatha A, et al. Statistical validation of image segmentation quality based on a spatial overlap index — Scientific reports. Acad Radiol 2004;11:178–189.

29. Roodink I, Leenders WPJ. Targeted therapies of cancer angiogenesis inhibition seems not enough. Cancer Lett 2010;299:1–10.

30. Farace P, Tambalo S, Fiorini S, et al. Early versus late GD-DTPA MRI enhancement in experimental glioblastomas. J Magn Reson Imaging 2011;33:550–556.

31. Blystad I, Warntjes JBM, Smedby O, Lundberg P, Larsson EM, Tisell A. Quantitative MRI for analysis of peritumoral edema in malignant gliomas. PLoS One 2017;12.

32. Machein MR, Plate KH. VEGF in brain tumors. J Neuro-Oncol 2000;50: 109–120.

33. Berkman RA, Merrill MJ, Reinhold WC, et al. Expression of the vascular-permeability factor vascular endothelial growth-factor gene in central-nervous-system neoplasms. J Clin Invest 1993;91:153–159.

34. Leenders WPJ, Kusters B, de Waal RMW. Vessel co-option: How tumors obtain blood supply in the absence of sprouting angiogenesis. Endothelium 2002;9:83–87.

35. Zhang Z, Jiang HH, Chen XZ, et al. Identifying the survival subtypes of glioblastoma by quantitative volumetric analysis of MRI. J Neuro-Oncol 2014;119:207–214.

36. Lin L, Xue YJ, Duan Q, et al. The role of cerebral blood flow gradient in peritumoral edema for differentiation of glioblastomas from solitary metastatic lesions. Oncotarget 2016;7:69051–69059.

37. Senger DR, Perruzzi CA, Feder J, Dvorak HF. A highly conserved vascular-permeability factor secreted by a variety of human and rodent tumor-cell lines. Cancer Res 1986;46:5629–5632.